



ELSEVIER

Available online at www.sciencedirect.com

SCIENCE @ DIRECT®

Earth and Planetary Science Letters 223 (2004) 381–393

EPSL

www.elsevier.com/locate/epsl

Equations of state of the high-pressure phases of a natural peridotite and implications for the Earth's lower mantle

Kanani K.M. Lee^{a,*}, Bridget O'Neill^{a,1}, Wendy R. Panero^{a,2}, Sang-Heon Shim^{a,3},
L. Robin Benedetti^{b,4}, Raymond Jeanloz^a

^aDepartment of Earth and Planetary Science, University of California, Berkeley, 307 McCone Hall, Berkeley, CA 94720-4767, USA

^bPhysics Department, University of California, Berkeley, 301 LeConte Hall, Berkeley, CA 94720-7300, USA

Received 24 September 2003; received in revised form 21 April 2004; accepted 30 April 2004

Abstract

To help determine the chemical composition of the Earth's mantle, we characterised the high-pressure mineral assemblage of an undepleted natural peridotite—thought to be representative of the Earth's upper-mantle—to 107 GPa using high-resolution X-ray diffraction. At lower-mantle conditions, the peridotite transforms to the assemblage 76 (± 2)% ($\text{Mg}_{0.88}\text{Fe}_{0.05}^{2+}\text{Fe}_{0.01}^{3+}\text{Al}_{0.12}\text{Si}_{0.94}$)O₃ orthorhombic perovskite by volume (at zero pressure), 17 (± 2)% ($\text{Mg}_{0.80}\text{Fe}_{0.20}$)O magnesiowüstite and 7 (± 1)% CaSiO₃ perovskite. The measured room-temperature bulk properties of this high-pressure assemblage, together with a range of estimates of thermal properties of the constituent minerals, appear to be inconsistent with seismological constraints on the density and bulk modulus of the lower mantle. Our results suggest that the lower mantle differs in bulk composition (e.g., richer in iron, Mg# ~ 0.85) from current estimates for the upper mantle, requiring some amount of segregation between the upper and lower mantle over geological history.

© 2004 Elsevier B.V. All rights reserved.

Keywords: peridotite; pyrolyte; orthorhombic perovskite; magnesiowüstite; calcium perovskite; high pressure; X-ray diffraction; lower mantle

1. Introduction

Geochemists, geodynamicists, seismologists and mineral physicists have long debated the nature of the Earth's mantle, which comprises more than three-quarters of our planet's volume and thus dictates the thermal and chemical evolution of the Earth [1–12]. The global discontinuities in seismic-wave velocities at 410 and 660 km depths are attributed to high-pressure transformations of upper-mantle minerals into lower-mantle phases [13–16]. However, various studies suggest that there may be large-scale compo-

* Corresponding author. Now at Division of Geological and Planetary Sciences, California Institute of Technology, 1200E. California Blvd. MC 170-25, Pasadena, CA 91125, USA.

E-mail address: kanani@gps.caltech.edu (K.K.M. Lee).

¹ Now at NPOI, Lowell Observatory, 1400 W. Mars Hill Rd., Flagstaff, AZ 86001, USA.

² Now at Department of Geological Sciences, University of Michigan, Ann Arbor, MI 48109, USA.

³ Now at Department of Earth, Atmospheric, and Planetary Sciences, Massachusetts Institute of Technology, 77 Massachusetts Avenue, 54-514, Cambridge, MA 02139, USA.

⁴ Now at European Synchrotron Radiation Facility, BP 220, 38043, Grenoble, France.

sitional variations near the base of the lower mantle, and there are reasons for suspecting that the mantle is not entirely uniform in bulk composition [8–10,17].

To assess the similarity in composition between the deep and shallower mantle, we compressed a natural peridotite—an upper-mantle rock—to lower-mantle pressures in a laser-heated diamond anvil cell, and measured the lattice parameters and compressibility of the various mineral phases by high-resolution synchrotron and laboratory-based X-ray diffraction. If the mantle is homogeneous, the density and elasticity of the upper-mantle rock composition, once transformed to the relevant mineral phases at lower-mantle conditions, should agree with the seismologically observed properties of the lower mantle.

2. Methods

The starting material for our experiment, BN-35 [18–20], is a garnet-spinel lherzolite from a xenolith, and is thought to be a good proxy for relatively primitive and fertile upper-mantle rock. With an Mg# \approx 0.89 and consisting of \sim 45% olivine, 25% orthopyroxene, 15% clinopyroxene and 15% garnet by volume [18,21], our sample is a natural analog of

pyrolite, a model composition intended to represent the upper mantle: see Table 1 (an Mg#, molar Mg/(Mg + Fe) ratio, of 0.90 (\pm 0.05) is the estimated value for the bulk composition of the uppermost mantle) [1].

Angle-dispersive X-ray diffraction patterns collected at high pressure, before and after laser heating, as well as after decompression confirm the identity of the phases, and show that their observed compressions are compatible with the known equations of state of the individual mineral phases (see Section 4). Two independent sets of experiments were carried out to document this conclusion. In the later set, samples were compressed and transformed under quasihydrostatic conditions (argon pressure medium) in a laser-heated diamond anvil cell (Nd-YAG laser, λ = 1064 nm or Nd-YLF laser, λ = 1053 nm), and characterised at room temperature by synchrotron X-ray diffraction using image plates at beamline 10–2 at the Stanford Synchrotron Radiation Laboratory (λ = 0.7277 Å) and the GSECARS 13-IDD beamline at the Advanced Photon Source (λ = 0.4246 Å). In the earlier set of experiments [19], the same sample material was loaded without a pressure medium and diffraction patterns were collected using laboratory sources with Mo K α (λ = 0.7107 Å) radiation (X-ray diffraction at high-pressure) and Cu K α (λ = 1.5418 Å) radiation (X-ray diffraction at

Table 1
Composition comparison of BN-35 and pyrolite

	BN-35 ^a cations per 12 O	Pyrolite ^b cations per 12 O ^c	Pyrolite ^d cations per 12 O	Upper mantle estimate ^e cations per 12 O ^c
Si	3.291 (0.094)	3.251 (0.084)	3.252	3.243 (0.101)
Ti	0.014 (0.008)	0.011 (0.011)		0.010 (0.003)
Al	0.367 (0.112)	0.391 (0.073)	0.375	0.382 (0.127)
Fe ^f	0.503 (0.072)	0.474 (0.101)	0.526	0.458 (0.102)
Mn	0.009 (0.002)	0.006 (0.002)		0.007 (0.003)
Mg	4.010 (0.128)	4.094 (0.235)	4.137	4.125 (0.215)
Ca	0.256 (0.012)	0.239 (0.065)	0.271	0.255 (0.077)
Na	0.042 (0.010)	0.056 (0.021)		0.057 (0.028)
K	0.0 (–)	0.002 (0.007)		0.001 (0.009)
Ni	0.014 (–)	0.012 (0.003)		0.013 (0.003)
Cr	0.017 (0.018)	0.017 (0.006)		0.023 (0.006)
Mg# = Mg/(Mg + Fe)	0.89	0.90 (0.05)	0.89	0.90 (0.05)

^a Uncertainties are given in parentheses and are determined by taking the difference of element values from an independent measurement of the starting sample [18,19].

^b An average pyrolite from Table 5-2, column 8 of [1]. Uncertainties are determined from the standard deviation of columns 1–7 of Table 5-2.

^c Uncertainties are given in parentheses.

^d A simplified model based on the five major oxide components [68].

^e From [69].

^f Fe²⁺ and Fe³⁺ totals are combined.

zero pressure). For each measurement in the early set of experiments (indicated by square symbols in Figs. 2–5), a different sample was loaded and compressed to the peak pressure; it was then heated and an X-ray diffraction pattern was taken at high pressure, after the sample had been heated and then cooled to room temperature. The sample was then decompressed to room pressure and a zero-pressure X-ray diffraction pattern was taken at room temperature. Ruby grains were added as a pressure calibrant in all experiments [22]. In some of the experimental runs, additional laser heating (at pressures of 41, 47, 66, 78 and 87 GPa in the latter set of experiments) was applied to thermally relax the sample of non-hydrostatic stresses. All X-ray diffraction measurements (synchrotron-and laboratory-based) were taken at 300 K, and the results are mutually compatible so that they are all used to compile a whole-rock equation of state. More detailed experimental procedures have been described elsewhere [19,20].

3. Experimental results

Upon compression to lower-mantle pressures ($P > 24$ GPa) and laser heating to ~ 2000 K in a diamond anvil cell, the peridotite transforms into a new assemblage consisting of $64 (\pm 2)$ mol% orthorhombic perovskite (opv), $31 (\pm 2)$ mol% magnesio-wüstite (mw) and $5 (\pm 1)$ mol% calcium perovskite (cpv). The identities of the high-pressure phases are determined by X-ray diffraction (Fig. 1), with the diffraction patterns analyzed both by individual fitting of peaks and by Rietveld refinement [19,20]. The relative abundances of the phases are determined through modeling the bulk composition of the starting material [20], and the results agree within experimental uncertainties with the relative abundances of phases obtained through Rietveld refinement of our powder diffraction patterns. Twenty-five X-ray diffraction patterns were taken of the sample at pressures between 25 and 107 GPa at room temperature, before

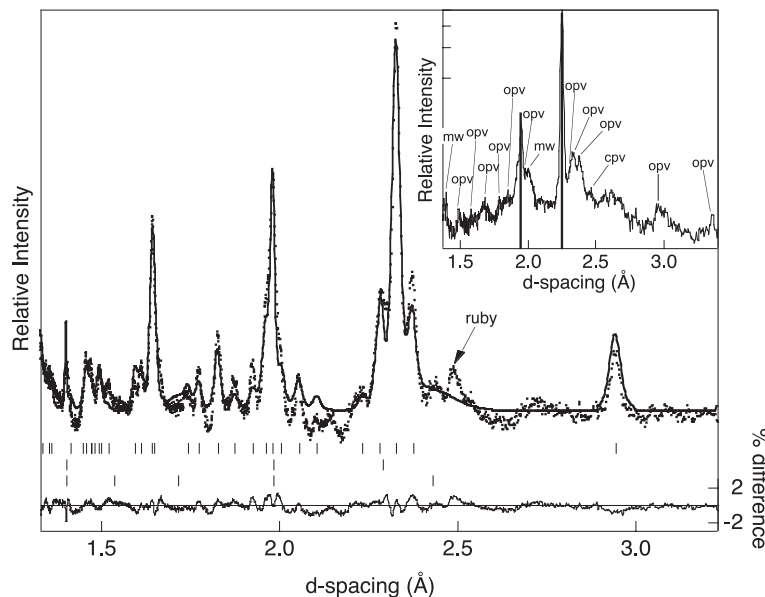


Fig. 1. Rietveld refinement applied to the powder-diffraction pattern of BN-35 at $59.5 (\pm 1.4)$ GPa and 300 K collected with synchrotron X-ray ($\lambda = 0.7277$ Å) radiation [20]. The raw data (dots) and the refinement (solid curve) are consistent with three phases: opv, mw, cpv (tick marks show theoretically expected positions of diffraction lines for these three phases in descending order). The unassigned diffraction peak at ~ 2.5 Å is attributed to ruby (internal pressure standard). The goodness of the fit is shown in the residuals (% difference between observed and Rietveld fit) plotted below the data. Inset: In-situ high-pressure and high-temperature energy-dispersive X-ray diffraction pattern shows the same phases to be present at $36 (\pm 2)$ GPa and $T \sim 1500 (\pm 150)$ K. Vertical lines denote the gold pressure calibrant and diffraction peaks from the individual phases are labeled.

and after heating, and upon subsequent decompression (see Fig. 1).

Additional in-situ high-pressure, high-temperature experiments confirm that the opv, mw and cpv phases exist at high temperatures (Fig. 1). Due to potential systematic errors, however, such measurements do not yield sufficiently reliable unit-cell volumes, hence bulk-rock density values, to allow a direct and independent comparison of the whole-rock assemblage at lower-mantle conditions with the seismologically observed properties of the mantle; therefore, the measurements obtained in situ, at simultaneously high pressures and temperatures, are not included here. The high-pressure and high-temperature data shown in the inset of Fig. 1 are nevertheless entirely consistent with our thermal equation of state discussed below.

3.1. Major-element partitioning

Major-element partitioning was determined from the observed ambient-pressure unit-cell volume V_0 of opv and mw, as well as analysis of the bulk (starting) composition of the rock assuming conservation of cations and charge. In the absence of other minor elements, Mg and Fe partitioning into these high-

pressure phases has been reasonably well documented [23–25], but the multi-variate partitioning of elements between the three phases found in the present natural assemblage is not well constrained by prior work [23,26,27]. No systematic trends in V_0 , and thus no systematic trends in individual phase compositions, were observed among our samples, despite different loading and synthesis conditions (e.g., pressure and temperature, see [20]). Therefore, the following assumptions were made in our analysis: the calcium perovskite is pure CaSiO_3 , incorporating all of the Ca in the multi-phase assemblage [27]; the Fe concentration in magnesiowüstite is determined by V_0 [14], with the remaining Fe assumed to be in orthorhombic perovskite; and all of the Al^{3+} cations are distributed between the Mg and Si sites in orthorhombic perovskite for charge balance. With the above constraints, it is possible to balance all major elements, yielding the assemblage composition: 64 (± 2) mol% orthorhombic perovskite ($\text{Mg}_{0.88}\text{Fe}_{0.05}\text{Fe}_{0.01}^{2+}\text{Al}_{0.12}\text{Si}_{0.94}\text{O}_3$), 31 (± 2) mol% magnesiowüstite ($\text{Mg}_{0.80}\text{Fe}_{0.20}\text{O}$) and 5 (± 1) mol% calcium perovskite CaSiO_3 . We note that the final values of whole-rock density remain unchanged, within quoted uncertainties, regardless of the validity of these assumptions (see [20], which also

Table 2

Comparison of equation of state parameters of lower-mantle minerals using a third order Birch-Murnaghan equation of state [54]

Study	Composition	V_0 (\AA^3)	K_{0T} (GPa)	K'_{0T}	P range (GPa)
<i>Orthorhombic perovskite</i>					
This study	$(\text{Mg}_{0.88}\text{Fe}_{0.05}^{2+}\text{Fe}_{0.01}^{3+}\text{Al}_{0.12}\text{Si}_{0.94})\text{O}_3$	163.90 (0.67)	269 (14)	4.06 (0.66)	24–107
Fiquet et al., 2000	MgSiO_3	162.27 (0.01)	253 (9)	3.9 (0.2)	39–94
Knittle and Jeanloz, 1987	$(\text{Mg}_{0.88}\text{Fe}_{0.12})\text{SiO}_3$	162.77 (0.39)	266 (6)	3.9 (0.4)	25–127
Mao et al., 1991	$(\text{Mg}_{1.00-0.80}\text{Fe}_{0.00-0.20})\text{SiO}_3$	162.49 (0.07)– 163.53 (0.10)	261 (4)	4.0 ^a	<29, synthesis at 40 GPa
Zhang and Weidner, 1999	$\text{Al}_{0.10}(\text{MgSi})_{0.95}\text{O}_3$	163.2 (0.2)	234 (4)	4.0 ^a	<10
Daniel et al., 2001	$\text{Al}_{0.154}(\text{MgSi})_{0.923}\text{O}_3$	163.52 (0.03)	229 (4)	2.5 (0.4)	<32
Andraut et al., 2001	$(\text{AlFe})_{0.05}(\text{MgSi})_{0.95}\text{O}_3$	163.2 (0.2)	265.0 (3.7)	4.0 ^a	26–58
Andraut et al., 2001	$\text{Al}_{0.05}\text{MgSi}_{0.95}\text{O}_3$	163.3 (0.2)	266.7 (2.8)	4.0 ^a	26–56
Andraut et al., 2001	$\text{Al}_{0.22}(\text{MgSi})_{0.89}\text{O}_3$	163.5 (0.4)	275.5 (6.0)	4.0 ^a	26–68
<i>Magnesiowüstite</i>					
This study	$(\text{Mg}_{0.80}\text{Fe}_{0.20})\text{O}$	76.09 (0.60)	175 (9)	3.75 (0.46)	24–107
Jackson and Niesler, 1982	MgO	74.69	162.5 (0.2)	4.13 (0.09)	<3
Duffy et al., 1995	MgO	74.7 ^a	177 (4)	4.0 (0.1)	<227
Dewaele et al., 2000	MgO	74.71 ^a	161 ^a	3.94 (0.2)	<53
Richet et al., 1989	$(\text{Mg}_{0.40}\text{Fe}_{0.60})\text{O}$	78.43 (0.02)	149 (4)	4.0 ^a	<50
Richet et al., 1989	$(\text{Mg}_{0.20}\text{Fe}_{0.80})\text{O}$	79.26 (0.03)	148 (10)	4.0 ^a	<49

^a Fixed.

summarizes electron probe microanalyses of our quenched samples).

4. High-pressure, room-temperature measurements

4.1. Orthorhombic perovskite

Orthorhombic perovskite has long been recognized as the most abundant phase in the Earth's mantle (e.g., [28,29]), probably making up more than 75% of the lower mantle and more than 50% of the Earth's volume. Except for a few early experiments on natural samples [19,21,29] and some recent experiments on Al-bearing perovskites [30–34], much of the focus has been on the Mg-endmember MgSiO_3 (e.g., [35]) and $(\text{Mg,Fe})\text{SiO}_3$ (e.g., [36]) (see Table 2). At all pressures in our experimental range, we observe orthorhombic perovskite and measure its unit-cell volume as a function of pressure

(Fig. 2). Despite a variety of synthesis-pressure and -temperature conditions, we do not find any systematic variations in Fe partitioning between opv and mw [20], although this has been previously proposed [24]. The fact that a single Fe/Mg distribution coefficient satisfactorily characterizes the opv and mw compositions in all of our runs, independent of equilibration (synthesis or annealing) pressure and temperature, may be due to our starting material being more complex (i.e., multi-component natural sample containing minor elements) than was the case in the previous studies on pure end-member samples (e.g., [37]).

Using a third order Birch-Murnaghan equation of state, we determined a compression curve for our opv and find that it is in good accord with previous equations of state (Table 2, Fig. 2). The relatively large V_0 that we measure for orthorhombic perovskite ($\sim 1\%$ larger than pure endmember MgSiO_3) is consistent with the results of past studies on Fe- and Al-bearing silicate perovskites [14,30,31], and the

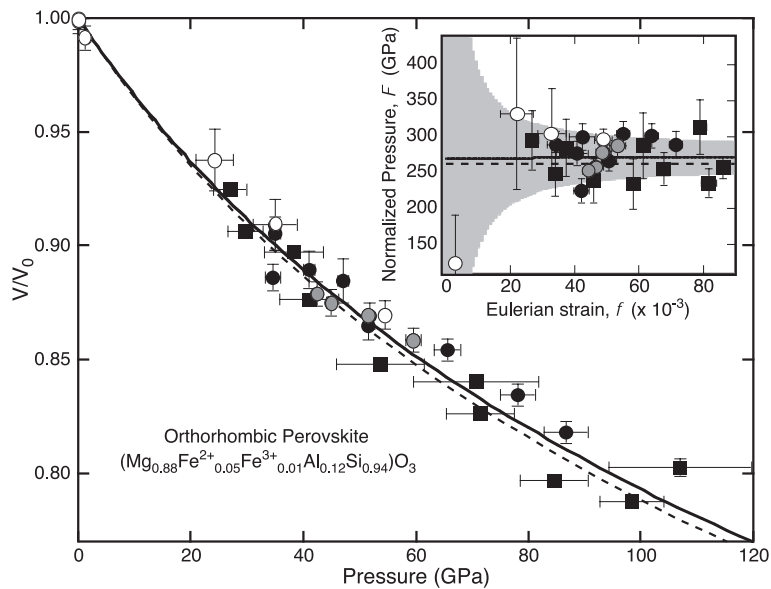


Fig. 2. Volume versus pressure for orthorhombic perovskite at room temperature, based on data collected both on compression with laser-annealing at each pressure (black) and decompression (white). Gray symbols are measurements done without laser-annealing after initial heating for synthesis. The circles are data collected from monochromatic ($\lambda = 0.7277 \text{ \AA}$) synchrotron radiation and the squares are from laboratory-based sources [20]. The heavy solid line through the data points is calculated from the Birch-Murnaghan equation of state. The dashed line is the Birch-Murnaghan equation of state of [36]. Inset: A more sensitive representation of the same data, an F vs. f plot (see Section 4.5, high-pressure, room-temperature measurements: Birch-Murnaghan equation of state). The intercept of the line is the K_{0T} ($269 \pm 14 \text{ GPa}$) of orthorhombic perovskite, while the slope is related to K'_{0T} (4.06 ± 0.66). The shaded area is the extrapolated uncertainty.

compressibility is compatible with that documented in [31] ($\sim 2\%$ smaller than pure endmember MgSiO_3). The effect of Al on the compressibility of orthorhombic perovskite has been the subject of much debate [30–32,38–41], although conflicting results may be due to different starting materials (Fe-bearing Mg-Al perovskites, glass vs. crystalline starting materials), synthesis conditions or one or more unknown parameters that have yet to be accounted for in experiments [41].

4.2. Magnesiowüstite

The second most dominant phase of the lower mantle is expected to be magnesiowüstite. Extensive work has been done on the pure Mg (e.g., [42–44]) and Fe (e.g., [45]) endmembers, as well as on a variety of compositions across the solid solution (e.g., [46,47]). Magnesiowüstite is observed at all our experimental pressures, as well as on quench, except at pressures of 70.6 and 84.4 GPa where the overlap of opv diffraction peaks obscures mw identification. The equation of state we determine is compatible

with those of former studies, as shown in Table 2 and Fig. 3.

4.3. Calcium perovskite

Calcium perovskite is thought to be the least abundant of the major phases in the Earth's lower mantle [48]. Due to the consequently weak diffraction peaks of calcium perovskite, and overlap of diffraction peaks with those of the more abundant phases, cpv was not detected above ~ 70 GPa even though its stability has been documented to much higher pressures [49,50] (Fig. 4). Calcium perovskite also does not quench to ambient conditions [49,50]. Although there is some spread in the reported compressibility of cpv [49,51,52], its low abundance (~ 5 mol%) means that any resulting uncertainties make little difference to the assemblage's bulk properties (e.g., $< 0.5\%$ effect on density). Because of these difficulties and the fact that our measurements are in agreement with it, the equation of state of [50] was used to determine the volume of the calcium perovskite portion of the assemblage in the modeling that we describe below.

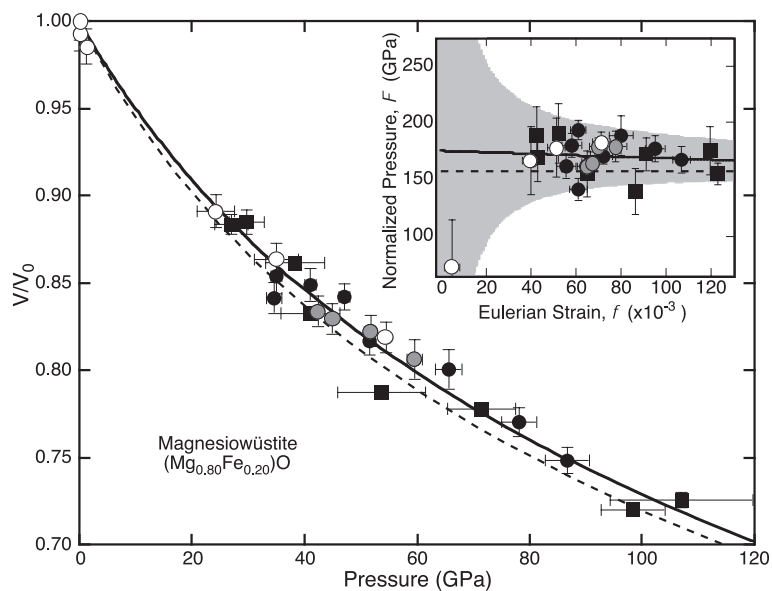


Fig. 3. Volume versus pressure for magnesiowüstite at room temperature. Symbol identification is the same as in Fig. 2. The heavy solid line through the data points is calculated from the Birch-Murnaghan equation of state. The dashed line is the Birch-Murnaghan equation of state of [46]. Inset: An F vs. f plot, as in Fig. 2. The intercept of the line is the K'_{0T} (175 ± 9 GPa) of magnesiowüstite, while the slope is related to K'_{0T} (3.75 ± 0.46).

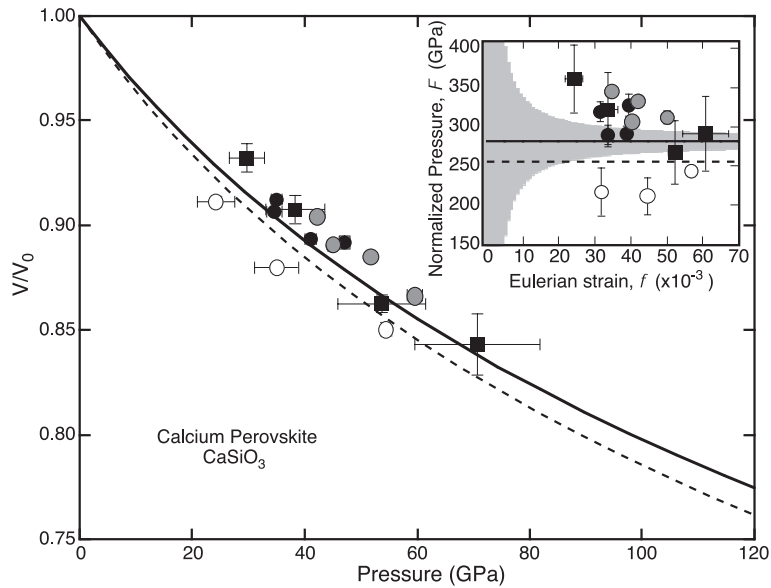


Fig. 4. Volume versus pressure for calcium perovskite at room temperature. Symbol identification is the same as in Fig. 2. The heavy solid line through the data points is calculated from the Birch-Murnaghan equation of state of [50] (used in the present study). For comparison, the dashed line is the equation of state measured by [51]. Inset: An F vs. f plot, as in Fig. 2.

4.4. Whole-rock assemblage

As we are able to track the structural changes of individual phases (see Tables 2 and 3), we are able to determine a high-pressure assemblage volume at each pressure, $V_{\text{BN-35}} = \sum x_i V_i$, from the molar ratios x_i of the three phases and the respective unit-cell volumes V_i (see Fig. 5). The density for the high-pressure assemblage is then calculated at each pressure from this assemblage volume and the known bulk composition of the sample.

The derivative of the pressure–volume relation for the high-pressure assemblage yields the isothermal bulk modulus of the rock as a function of pressure (therefore depth) in the mantle. Other methods of determining the bulk compressional properties of composite materials include the Reuss (all grains equally stressed) and Voigt (all grains equally strained) approximations (see [53] for a review); these provide a measure of the uncertainty associated with averaging the moduli (Table 3). The arithmetic mean of the Voigt and Reuss bounds, the Voigt–Reuss–Hill average, has also been suggested as another approximation to the moduli of composite materials. Whichever approximation is invoked (they all lie within mutual uncertain-

ties), none of our conclusions regarding the density and bulk composition of the lower mantle is affected. Also dispersion is known to affect the seismologically

Table 3

Equation of state data for the three high-pressure phases and the whole-rock assemblage observed for a peridotite composition at lower-mantle pressures^a

Phase	V_0 (\AA^3)	K_{0T} (GPa)	K'_{0T}	x_i (mol%)
opv	163.90 (0.67)	269 (14)	4.06 (0.66)	64 (2)
mw	76.09 (0.60)	175 (9)	3.75 (0.46)	31 (2)
cpv ^b	45.37 (0.08)	281 (4)	4.0	5 (1)
Whole rock				
Constant, mol%		247 (21)	4.01 (0.67)	
Reuss		247 (15)	4.13 (0.48)	
Voigt		254 (11)	4.00 (0.51)	
Voigt–Reuss–Hill		251	4.07	

Listed are the measured V_0 , K_{0T} , K'_{0T} and mol% of each of the three lower-mantle phases, as well as the whole-rock bulk properties obtained by four methods for calculating the properties of multiphase assemblages [53]. We assume that the given phases keep a constant mol% abundance throughout the mantle, which yields $K_{0T} = 247 (\pm 21)$ GPa and $K'_{0T} = 4.01 (\pm 0.67)$. The other methods (Reuss, Voigt and Voigt–Reuss–Hill) all yield values that fall within quoted uncertainties of our assumption of constant molar abundance.

^a Uncertainties in parentheses are 2 standard deviations.

^b Values taken from [50], where K'_{0T} is constrained to 4.0.

observed moduli, which are only partly relaxed, whereas our approach yields fully relaxed values. Therefore, our calculated bulk modulus represents a lower bound for comparison with the mantle and may systematically underestimate the seismologically observed modulus. In combination with the effects of averaging moduli for a poly-phase aggregate, the resultant offset can amount to as much as 3% increased stiffness at lower-mantle conditions.

4.5. Birch-Murnaghan equation of state

The individual-phase isothermal bulk modulus, K_{0T} , and its pressure derivative, K'_{0T} , are determined using the Birch-Murnaghan formalism [54], a good approximation for Earth materials that is based on a Taylor expansion of the Helmholtz free energy in the Eulerian strain measure:

$$f = \frac{1}{2} \left[\left(\frac{V}{V_0} \right)^{-2/3} - 1 \right] \quad (1)$$

where V/V_0 is the ratio of the high-pressure volume V to the room-pressure volume V_0 . The pressure P can

be normalized to give an effective derivative of the equation of state:

$$F = \frac{P}{3f(1+2f)^{5/2}} \quad (2)$$

Expanding to fourth order in Eulerian strain,

$$F = K_{0T} \left(1 + f \left(\frac{3}{2} K'_{0T} - 6 \right) + f^2 \left(\frac{3}{2} K_{0T} K''_{0T} + \frac{3}{2} K'_{0T} (K'_{0T} - 7) + \frac{143}{6} \right) + \dots \right) \quad (3)$$

Routinely, the Birch-Murnaghan formalism is truncated to third order (before the f^2 term), hence an F vs. f plot yields K_{0T} (intercept) and K'_{0T} (via the slope) (see insets of Figs. 2–5).

5. High-temperature analysis

5.1. Whole-rock assemblage at high pressure and temperature

To compare our whole-rock, room-temperature data with seismic observations of the Earth's interior, we

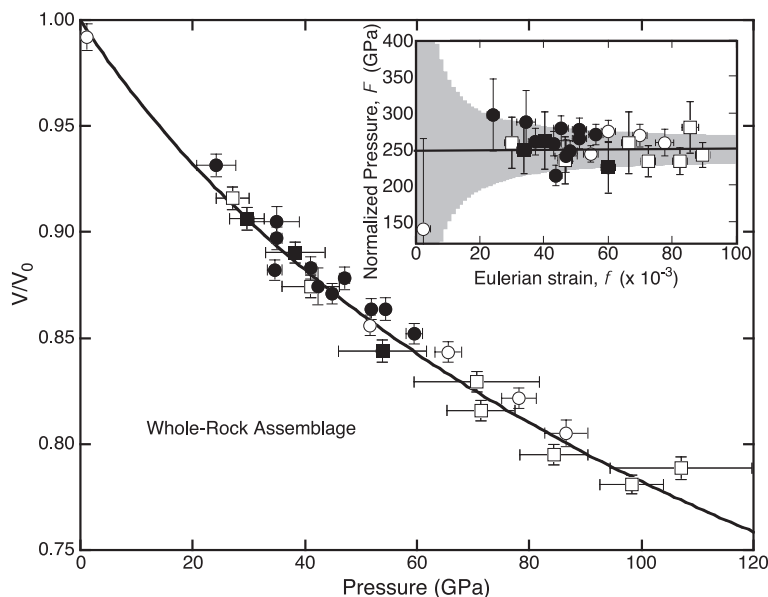


Fig. 5. Volume versus pressure for the transformed peridotite assemblage at room temperature, based on data collected both on compression and decompression. The circles are data collected from synchrotron radiation [20] and the squares are from laboratory-based sources [19,21]. The solid shapes represent diffraction patterns in which all three phases are present, while the open shapes include extrapolation due to unobserved phases. The curve through the data points is calculated from the Birch-Murnaghan equation of state of the whole-rock assemblage. Inset: An F vs. f plot, as in Fig. 2. The intercept of the line is the K_{0T} (247 ± 21 GPa) of the rock, while the slope is related to K'_{0T} (4.01 ± 0.67).

applied a Mie–Grüneisen–Debye model to determine a thermal equation of state for each phase as well as for the whole-rock assemblage at temperatures of 1000, 1500, 2000, 2500 and 3000 K (Fig. 6) (see Section 5.2). Because the temperature variation is expected to be small across the bulk of the lower mantle (~ 500 K

from about 700 to 2700 km depth), an isotherm is a reasonable approximation for the actual temperature variation throughout much of the deep interior [55,56]. Two sets of thermal parameters are used to compare our thermally corrected data with the Preliminary Reference Earth Model (PREM) [57] (Table 4): the “Stan-

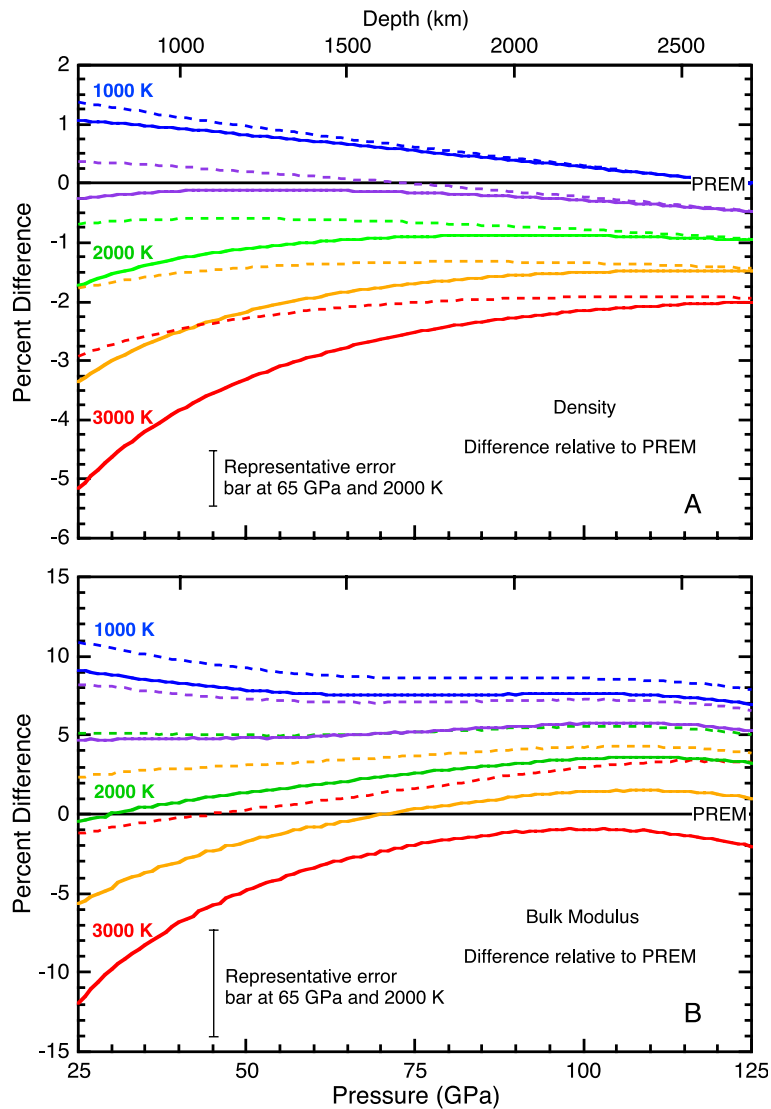


Fig. 6. Comparison of lower-mantle assemblage with PREM [57]. Results for two thermal equations of state are plotted, which give a range of possibilities for mantle thermal expansivities: standard (solid) and low (dash) thermal expansion parameters (see Table 4). The isothermal temperatures used in the model are 1000 K (blue), 1500 K (purple), 2000 K (green), 2500 K (orange) and 3000 K (red). Representative error bars at 65 GPa (~ 1500 km depth) and 2000 K are given (see Section 5.3, high-temperature analysis: high-temperature error analysis). (A) At temperatures relevant to the lower mantle of the Earth (2000–3000 K), the density of the whole-rock assemblage is lower than that of PREM by 1–4%. (B) The adiabatic bulk modulus K_s also differs from PREM by up to $\sim 3\%$ for relevant lower-mantle temperatures.

Table 4
Thermal parameters used in or obtained from the Mie–Grüneisen–Debye equation of state

“Standard” thermal expansion parameters				
	opv ^a	mw ^b	cpv ^c	Rock ^d
Θ_D (K)	1017	500	1100	
γ_0	1.96	1.5	1.7	
q	2.5	1.1	1	
$\alpha_{300\text{ K}, 0\text{ GPa}} (10^{-5}\text{ K})$	2.4	3.1	3.0	2.6
$\alpha_{2000\text{ K}, 0\text{ GPa}} (10^{-5}\text{ K})^d$	6.8	5.0	3.4	6.3
$\alpha_{2000\text{ K}, 25\text{ GPa}} (10^{-5}\text{ K})^d$	3.3	2.9	2.3	3.2
“Low” thermal expansion parameters				
	opv ^e	mw ^e	cpv ^e	Rock ^d
Θ_D (K)	1000	673	1100	
γ_0	1.31	1.41	1.7	
q	1	1.3	1	
$\alpha_{300\text{ K}, 0\text{ GPa}} (10^{-5}\text{ K})$	1.6	3.1	3.0	2.0
$\alpha_{2000\text{ K}, 0\text{ GPa}} (10^{-5}\text{ K})^d$	3.0	4.8	3.4	3.3
$\alpha_{2000\text{ K}, 25\text{ GPa}} (10^{-5}\text{ K})^d$	2.1	2.6	2.3	2.2

^a From [9].

^b From [46].

^c From [52].

^d Calculated values (see Section 5.2, High-temperature analysis: Thermal equation of state).

^e From [6].

“Low” set [46,52,58] is supported by a reanalysis of the gold pressure standard [59], whereas the “Standard” set is illustrative of prior analyses yielding relatively low values of thermal expansion [6].

5.2. Thermal equation of state

A Mie–Grüneisen thermal equation of state adds a thermal pressure to the room-temperature pressure at a given volume, yielding a total pressure at temperature T [6,60]:

$$P_{\text{total}}(V, T) = P(V, 300\text{ K}) + P_{\text{thermal}}(V, T) \quad (4)$$

where,

$$P_{\text{thermal}} = \left(\frac{\gamma}{V}\right) [E_{\text{thermal}}(T, \Theta_D) - E_{\text{thermal}}(300\text{ K}, \Theta_D)] \quad (5)$$

where the Grüneisen parameter, γ , is,

$$\gamma = \gamma_0 \left(\frac{V}{V_0}\right)^q = -\frac{\partial \ln \Theta_D}{\partial \ln V} \quad (6)$$

and with a Debye model for the internal energy, E_{thermal} ,

$$E_{\text{thermal}} = 9nRT \left(\frac{T}{\Theta_D}\right)^3 \int_0^{\frac{\Theta_D}{T}} \frac{x^3 dx}{e^x - 1} \quad (7)$$

and

$$\Theta_D = \Theta_{D0} \exp\left(\frac{\gamma_0 - \gamma}{q}\right), \quad (8)$$

where Θ_D is the Debye temperature. Subscript 0 indicates a value at zero pressure and 300 K. The correction from isothermal to adiabatic (subscript S) bulk modulus, $K_S = K_T(1 + \alpha\gamma T)$, is performed in a self-consistent manner using the same model and individual phase parameters (α is the volumetric thermal-expansion coefficient). K_T is determined from the fourth-order Birch-Murnaghan equation of state (Eq. (3)) [54]. For the whole-rock assemblage, we use $\gamma_{\text{rock}} = \sum a_i \gamma_i$, where a_i is the volume percent of each phase and γ_i is the phase Grüneisen parameter. As thermal expansion depends on both pressure and temperature, we solved for α_{rock} directly by solving for the volume of the rock (as stated above) for a small interval (± 1 K) around the temperature of interest and using $(\alpha = \frac{\partial \ln V}{\partial T})_P$ (Table 4).

5.3. High-temperature error analysis

Representative error bars for the final pressure at a given volume and temperature are derived from the uncertainties in the 300 K compression measurements and in the correction to high temperature. The uncertainty in compression is determined via Bell et al.’s analysis [61], while the uncertainty in the thermal correction is based on the difference between the standard and low thermal-expansion models (Fig. 6, Table 4). This determination of uncertainty is probably generous, as the thermal portion (~ 2 times the compression part of the uncertainty) encompasses the full range of possible temperature corrections (“standard” and “low” thermal expansion parameters, Table 4).

In general, at a given pressure an increase in temperature increases the uncertainty in the thermal contribution to the equation of state; conversely, at a given temperature, an increase in pressure decreases the magnitude of the uncertainty in the thermal

portion of the equation of state. The reason for this is that the absolute magnitude of the thermal correction to the 300 K pressure (at a given volume) increases with increasing temperature and decreases with increasing pressure, the latter mitigating the increase in *relative* uncertainty of the thermal correction with increasing pressure.

6. Discussion

We apply our results by first testing the hypothesis that the entire mantle is uniformly mixed and consists of a pyrolite-like composition. Comparison of experimentally observed phase transformations with the corresponding depths of seismic discontinuities within the transition zone yields a temperature of 1900–2000 K for the top of the lower mantle, rising toward 2500 K at the bottom assuming an adiabat [14–16,62].

It is evident from Fig. 6A, however, that the density of our natural peridotite is incompatible with such high temperatures. Even accounting for uncertainties in the thermal properties, the density can only be matched by invoking temperatures between 1000 and 1500 K across the depth of the lower mantle: about 1000 K too cold, and below typical eruption temperatures at mid-ocean ridges [63]. Indeed, analysis of the bulk modulus also suggests lower-mantle temperatures in the range of 2000–3000 K (Fig. 6B).

One way to satisfy the observed properties of the lower mantle with a peridotite-like composition close to that which we studied is to invoke a higher iron content at depth, rather than the preferred value for the upper mantle ($Mg\# \approx 0.90$, see Table 1). If some region of the deep mantle differs in bulk composition from the shallower mantle, however, then temperatures are expected to be increased by about 500–1000 K due to the presence of thermal boundary layers at the interface at which the bulk composition changes, across which mixing is suppressed [56]. Thus, temperatures of about 2500–3000 (± 500) K are reasonable for a layer within the lower mantle that differs in composition from shallower depths (e.g., [8]).

As varying the Fe/Mg ratio has essentially no effect on the bulk modulus of the high-pressure, perovskite-dominated assemblage (e.g., [36]), Fig. 6B shows that such high temperatures are in good

accord with our measurements. The density deficit of ~ 1 –4% obtained from Fig. 6A can then be “fixed” by an increased abundance of iron, to an $Mg\# \approx 0.85$ (± 0.02). The result is non-unique, however, as there are tradeoffs between temperature and composition (e.g., including Si, Al and Ca abundances) for satisfying the observed properties of the lower mantle [9,58]. In particular, the detailed amounts as well as compositions of mw relative to opv depend on at least the abundances of Fe and Si (e.g., relative to Mg).

Nevertheless, the intrinsic density difference between the observed density profile for the lower mantle and the lower-mantle density predicted for the current (pyrolite-like) estimate of upper-mantle bulk composition is sufficient to stabilize layered convection over geological time [64–67]. Thus, geochemical, geophysical and, now, mineral physical observations point to complex structure and dynamics of the Earth’s mantle [8].

Acknowledgements

This work was supported by NSF, NASA, DOE and the University of California’s Miller Institute for Basic Research in Science. We thank M.S.T. Bukowski, A.M. Jellinek, J. Korenaga and M. Manga for helpful discussions, and G. Shen for experimental assistance. We thank Carl Agee for constructive comments that helped us clarify our results. Portions of this research were carried out at the Stanford Synchrotron Radiation Laboratory, a national user facility operated by Stanford University on behalf of the U.S. Department of Energy, Office of Basic Energy Sciences. Use of the Advanced Photon Source was supported by the U. S. Department of Energy, Office of Basic Energy Sciences, under Contract No. W-31-109-Eng-38. [KF]

References

- [1] A.E. Ringwood, *Composition and Petrology of the Earth’s Mantle*, McGraw-Hill, New York, 1975, 618 pp.
- [2] D.P. McKenzie, J.M. Roberts, N.O. Weiss, Convection in the Earth’s mantle: towards a numerical simulation, *Journal of Fluid Mechanics* 62 (Pt. 3) (1974) 465–538.
- [3] D.L. Anderson, *Composition of the Earth*, *Science* 243 (1989) 367–370.

- [4] Y. Fukao, S. Widiyantoro, M. Obayashi, Stagnant slabs in the upper and lower mantle transition region, *Reviews of Geophysics* 39 (3) (2001) 291–323.
- [5] G.R. Helffrich, B.J. Wood, The Earth's mantle, *Nature* 412 (6846) (2001) 501–507.
- [6] I. Jackson, Elasticity, composition and temperature of the Earth's lower mantle: a reappraisal, *Geophysical Journal International* 134 (1) (1998) 291–311.
- [7] R. Jeanloz, E. Knittle, Density and composition of the lower mantle, *Philosophical Transactions of the Royal Society of London, Series A: Mathematical and Physical Sciences* 328 (1599) (1989) 377–389.
- [8] L.H. Kellogg, B.H. Hager, R.D. van der Hilst, Compositional stratification in the deep mantle, *Science* 283 (5409) (1999) 1881–1884.
- [9] L. Stixrude, R.J. Hemley, Y. Fei, et al., Thermoelasticity of silicate perovskite and magnesiowüstite and stratification of the Earth's mantle, *Science* 257 (5073) (1992) 1099–1101.
- [10] R.D. van der Hilst, H. Karason, Compositional heterogeneity in the bottom 1000 kilometers of Earth's mantle: toward a hybrid convection model, *Science* 283 (5409) (1999) 1885–1888.
- [11] P.E. van Keken, E.H. Hauri, C.J. Ballentine, Mantle mixing: the generation, preservation, and destruction of chemical heterogeneity, *Annual Reviews of Earth and Planetary Science* 30 (11) (2002) 1–33.
- [12] M.J. Drake, K. Righter, Determining the composition of the Earth, *Nature* 416 (2002) 39–44.
- [13] C.B. Agee, Phase transformation and seismic structure in the upper mantle and transition zone, in: R.J. Hemley (Ed.), *Ultrahigh-Pressure Mineralogy: Physics and Chemistry of the Earth's Deep Interior*, *Reviews in Mineralogy*, vol. 37, Mineralogical Society of America, Washington, DC, 1998, pp. 165–203.
- [14] R. Jeanloz, A.B. Thompson, Phase transitions and mantle discontinuities, *Reviews of Geophysics and Space Physics* 21 (1) (1983) 51–74.
- [15] S.H. Shim, T.S. Duffy, G. Shen, The post-spinel transformation in Mg_2SiO_4 and its relation to the 660 km seismic discontinuity, *Nature* 411 (6837) (2001) 571–574.
- [16] I. Chudinovskikh, R. Boehler, High-pressure polymorphs of olivine and the 660-km seismic discontinuity, *Nature* 411 (6837) (2001) 574–577.
- [17] A.M. Forte, J.X. Mitrovica, Deep-mantle high-viscosity flow and thermochemical structure inferred from seismic and geodynamic data, *Nature* 410 (6832) (2001) 1049–1056.
- [18] C.R. Stern, S.L. Saul, M.A. Skewes, et al., Garnet peridotite xenoliths from the Pali-Aike alkali basalts of southernmost South America, in: J. Ross (Ed.), *Fourth International Kimberlite Conference, Kimberlites and Related Rocks*, vol. 2, Blackwell, Perth, Australia, 1986, pp. 735–744.
- [19] B. O'Neill, *Experimental Petrology of the Lower Mantle*, PhD, University of California, Berkeley, 1994.
- [20] K.K.M. Lee, B. O'Neill, R. Jeanloz, Limits to resolution in composition and density in ultrahigh-pressure experiments on natural mantle-rock samples, *Physics of the Earth and Planetary Interiors* 143–144 (2004) 241–253.
- [21] B. O'Neill, R. Jeanloz, Experimental petrology of the lower mantle: a natural peridotite taken to 54 GPa, *Geophysical Research Letters* 17 (10) (1990) 1477–1480.
- [22] H.K. Mao, P.M. Bell, J.W. Shaner, et al., Specific volume measurements of Cu, Mo, Pd, and Ag and calibration of the ruby R1 fluorescence pressure gauge from 0.06 to 1 Mbar, *Journal of Applied Physics* 49 (6) (1978) 3276–3283.
- [23] B. O'Neill, R. Jeanloz, MgSiO_3 – FeSiO_3 – Al_2O_3 in the Earth's lower mantle: perovskite and garnet at 1200 km depth, *Journal of Geophysical Research* 99 (B10) (1994) 19901–19915.
- [24] H.K. Mao, G. Shen, R.J. Hemley, Multivariable dependence of Fe–Mg partitioning in the lower mantle, *Science* 278 (5346) (1997) 2098–2100.
- [25] D. Andraut, Evaluation of (Mg,Fe) partitioning between silicate perovskite and magnesiowüstite up to 120 GPa and 2300 K, *Journal of Geophysical Research* 106 (B2) (2001) 2079–2087.
- [26] B.J. Wood, D.C. Rubie, The effect of alumina on phase transformations at the 660-kilometer discontinuity from Fe–Mg partitioning experiments, *Science* 273 (5281) (1996) 1522–1524.
- [27] B.J. Wood, Phase transformations and partitioning relations in peridotite under lower mantle conditions, *Earth and Planetary Science Letters* 174 (3–4) (2000) 341–354.
- [28] L.G. Liu, Orthorhombic perovskite phases observed in olivine, pyroxene, and garnet at high pressures and temperatures, *Physics of the Earth and Planetary Interiors* 11 (1976) 289–298.
- [29] E. Knittle, R. Jeanloz, Synthesis and equation of state of (Mg,Fe) SiO_3 perovskite to over 100 gigapascals, *Science* 235 (4789) (1987) 668–670.
- [30] I. Daniel, H. Cardon, G. Fiquet, et al., Equation of state of Al-bearing perovskite to lower mantle pressure conditions, *Geophysical Research Letters* 28 (19) (2001) 3789–3792.
- [31] D. Andraut, N. Bolfan-Casanova, N. Guignot, Equation of state of lower mantle (Al,Fe)– MgSiO_3 perovskite, *Earth and Planetary Science Letters* 193 (3–4) (2001) 501–508.
- [32] J. Zhang, D.J. Weidner, Thermal equation of state of aluminum-enriched silicate perovskite, *Science* 284 (1999) 782–784.
- [33] Y. Xu, C. McCammon, B.T. Poe, The effect of alumina on the electrical conductivity of silicate perovskite, *Science* 282 (5390) (1998) 922–924.
- [34] D.J. Frost, F. Lagenhorst, The effect of Al_2O_3 on Fe–Mg partitioning between magnesiowüstite and magnesium silicate perovskite, *Earth and Planetary Science Letters* 199 (2002) 227–241.
- [35] G. Fiquet, A. Dewaele, D. Andraut, et al., Thermoelastic properties and crystal structure of MgSiO_3 perovskite at lower mantle pressure and temperature conditions, *Geophysical Research Letters* 27 (1) (2000) 21–24.
- [36] H.K. Mao, R.J. Hemley, Y. Fei, et al., Effect of pressure, temperature, and composition on lattice parameters and density of (Fe,Mg) SiO_3 -perovskites to 30 GPa, *Journal of Geophysical Research* 96 (B5) (1991) 8069–8079.
- [37] Y. Fei, Solid solutions and element partitioning at high pressures and temperatures, in: R.J. Hemley (Ed.), *Ultrahigh-Pressure Mineralogy: Physics and Chemistry of the Earth's Deep Interior*, *Reviews in Mineralogy*, vol. 37, Mineralogical Society of America, Washington, DC, 1998, pp. 343–367.

- [38] S. Akber-Knutson, M.S.T. Bukowski, The energetics of aluminum solubility into MgSiO_3 perovskite at lower mantle conditions, *Earth and Planetary Science Letters* 7014 (2004) 1–14.
- [39] A. Kubo, T. Yagi, S. Ono, et al., Compressibility of $\text{Mg}_{0.9}\text{Al}_{0.2}\text{Si}_{0.9}\text{O}_3$ perovskite, *Proceedings of the Japan Academy. Series B Physical and Biological Sciences* 76 (8) (2000) 103–107.
- [40] M.J. Walter, A. Kubo, T. Yoshino, J. Brodholt, K.T. Koga, Y. Ohishi, Phase relations and equation-of-state of aluminous Mg-silicate perovskite and implications for Earth's lower mantle, *Earth and Planetary Science Letters* 222 (2004) 501–516.
- [41] T. Yagi, K. Okabe, N. Nishiyama, Complicated effects of aluminum on the compressibility of silicate perovskite, *Physics of the Earth and Planetary Interiors* 143–144 (2004) 81–91.
- [42] A. Dewaele, G. Fiquet, D. Andrault, et al., P–V–T equation of state of periclase from synchrotron radiation measurements, *Journal of Geophysical Research* 105 (B2) (2000) 2869–2877.
- [43] I. Jackson, H. Niesler, The elasticity of periclase to 3 GPa and some geophysical implications, in: S. Akimoto, M.H. Manghnani (Eds.), *Center for Academic Publications*, 1982, pp. 93–113.
- [44] T.S. Duffy, R.J. Hemley, H.K. Mao, Equation of state and shear strength at multimegabar pressures: magnesium oxide to 227 GPa, *Physical Review Letters* 74 (1995) 1371–1374.
- [45] R.M. Hazen, R. Jeanloz, Wüstite (Fe_{1-x}O): a review of its defect structure and physical properties, *Reviews of Geophysics and Space Physics* 22 (1) (1984) 37–46.
- [46] Y. Fei, H.-K. Mao, J. Shu, et al., P–V–T equation of state of magnesiowüstite ($\text{Mg}_{0.6}\text{Fe}_{0.4}\text{O}$), *Physics and Chemistry of Minerals* 18 (1992) 416–422.
- [47] P. Richet, M. Ho-Kwang, P.M. Bell, Bulk moduli of magnesiowüstites from static compression measurements, *Journal of Geophysical Research* 94 (B3) (1989) 3037–3045.
- [48] S.H. Shim, T.S. Duffy, G. Shen, The stability and P–V–T equation of state of CaSiO_3 perovskite in the Earth's lower mantle, *Journal of Geophysical Research* 105 (B11) (2000) 25955–25968.
- [49] S.-H. Shim, T.S. Duffy, G. Shen, The equation of state of CaSiO_3 perovskite to 108 GPa at 300 K, *Physics of the Earth and Planetary Interiors* 120 (4) (2000) 327–338.
- [50] H.K. Mao, L.C. Chen, R.J. Hemley, et al., Stability and equation of state of CaSiO_3 -perovskite to 134 GPa, *Journal of Geophysical Research* 94 (B12) (1989) 17889–17894.
- [51] S.H. Shim, R. Jeanloz, T.S. Duffy, Tetragonal structure of CaSiO_3 perovskite above 20 GPa, *Geophysical Research Letters* 29 (24) (2002) 2166.
- [52] Y. Wang, D.J. Weidner, F. Guyot, Thermal equation of state of CaSiO_3 perovskite, *Journal of Geophysical Research* 101 (B1) (1996) 661–672.
- [53] F.D. Stacey, Thermoelasticity of a mineral composite and a reconsideration of lower mantle properties, *Physics of the Earth and Planetary Interiors* 106 (3–4) (1998) 219–236.
- [54] F. Birch, Finite strain isotherm and velocities for single-crystal and polycrystalline NaCl at high pressures and 300 K, *Journal of Geophysical Research* 83 (1978) 1258–1267.
- [55] J.M. Brown, T.J. Shankland, Thermodynamic parameters in the Earth as determined from seismic profiles, *Geophysical Journal of the Royal Astronomical Society* 66 (3) (1981) 579–596.
- [56] R. Jeanloz, F.M. Richter, Convection, composition, and the thermal state of the lower mantle, *Journal of Geophysical Research* 84 (B10) (1979) 5497–5504.
- [57] A.M. Dziewonski, D.L. Anderson, Preliminary reference Earth model, *Physics of the Earth and Planetary Interiors* 25 (4) (1981) 297–356.
- [58] L. Stixrude, M.S.T. Bukowski, Stability of $(\text{Mg,Fe})\text{SiO}_3$ perovskite and the structure of the lowermost mantle, *Geophysical Research Letters* 19 (10) (1992) 1057–1060.
- [59] S.H. Shim, T.S. Duffy, K. Takemura, Equation of state of gold and its application to the phase boundaries near 660-km depth in the Earth's mantle, *Earth and Planetary Science Letters* 203 (2) (2002) 729–739.
- [60] I. Jackson, S.M. Rigden, Analysis of P–V–T data: constraints on the thermoelastic properties of high-pressure minerals, *Physics of the Earth and Planetary Interiors* 96 (1996) 85–112.
- [61] P.M. Bell, H.K. Mao, J.A. Xu, Error analysis of parameter-fitting in equations of state for mantle minerals, in: M.H. Manghnani, Y. Syono (Eds.), *High-Pressure Research in Mineral Physics*, vol. 2, American Geophysical Union, Washington, DC, 1987, pp. 447–454.
- [62] E. Ito, E. Takahashi, Postspinel transformations in the system Mg_2SiO_4 – Fe_2SiO_4 and some geophysical implications, *Journal of Geophysical Research* 94 (1989) 10637–10646.
- [63] C.R.J. Kilburn, Lava flows and flow fields, in: H. Sigurdsson (Ed.), *Encyclopedia of Volcanoes*, Academic Press, San Diego, 2000, pp. 291–305.
- [64] U.R. Christensen, Models of mantle convection: one or several layers, *Philosophical Transactions of the Royal Society of London, Series A: Mathematical and Physical Sciences* 328 (1989) 417–424.
- [65] P. Olson, An experimental approach to thermal convection in an two-layered mantle, *Journal of Geophysical Research* 89 (1984) 11293–11301.
- [66] F.M. Richter, D.P. McKenzie, On some consequence and possible causes of layered mantle convection, *Journal of Geophysical Research* 86 (1981) 6133–6142.
- [67] H. Gonnerman, M. Manga, A.M. Jellinek, Dynamics and longevity of an initially stratified mantle, *Geophysical Research Letters* 29 (10) (2002) 1399.
- [68] I. Jackson, *The Earth's Mantle: Composition, Structure, and Evolution*, Cambridge Univ. Press, Cambridge, UK, 1998, p. 566.
- [69] R. Jeanloz, The Earth's Mantle, in: H. Sigurdsson (Ed.), *Encyclopedia of Volcanoes*, Academic Press, San Diego, 2000, p. 41.